ACS APPLIED MATERIALS & INTERFACES

www.acsami.org

Research Article

Interface-Engineered $NiSe_2$/Ni−Fe_2P Nanocubes for Efficient and Durable Seawater Electrolysis

Huiya Zhou, Xin Li, Boyao Zhang, Heran Ren, Depeng Zhao,* Rongda Zhao,* and Lihua Miao*

Cite This: *ACS Appl. Mater. Interfaces* 2025, 17, 64340−64353

Read Online

ACCESS | Metrics & More | Article Recommendations | Supporting Information

ABSTRACT: Seawater electrolysis technology holds significant potential for efficient utilization of abundant seawater resources. However, its practical application is constrained by impurity interference in seawater and chlorine gas evolution during the oxygen evolution reaction (OER). To address these challenges, we employed a self-sacrificial template strategy using $NiSe_2$/NF as the sacrificial template. The etching effect of $K_3[Fe(CN)_6]$ induced interfacial reactions to in situ synthesize $NiSe_2$@NiFe-PBA nanoboxes, which were subsequently transformed into nanocube spherical morphologies ($NiSe_2$/Ni−Fe_2P) through vapor-phase phosphidation. The $NiSe_2$/Ni−Fe_2P catalyst demonstrates an excellent OER performance in alkaline seawater, requiring an ultralow overpotential of 281 mV to achieve 100 mA cm^{-2}, coupled with a remarkable stability exceeding 100 h. When integrated into a full water-splitting system, the electrolyzer delivers 100 mA cm^{-2} at only 1.854 V, maintaining stability for over 200 h. Comprehensive evaluation of the hydrogen evolution reaction (HER) performance across all samples revealed that the $NiSe_2$@NiFe-PBA/NF catalyst achieved a current density of −10 mA cm^{-2} at an overpotential of 168 mV in 1.0 M KOH electrolyte. Further DFT calculations demonstrated that compared to pure-phase $NiSe_2$, the $NiSe_2$@NiFe-PBA heterostructure effectively modulated surface hydrogen adsorption energy and reduced the HER reaction barrier, thereby significantly enhancing the catalytic activity.

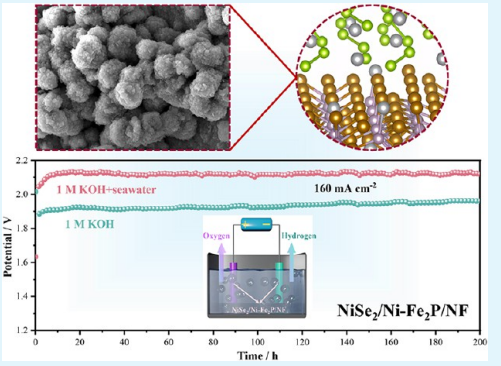

KEYWORDS: *seawater electrolysis, oxygen evolution reaction (OER), $NiSe_2$/Ni−Fe_2P, hydrogen evolution reaction (HER), water splitting*

1. INTRODUCTION

As fossil energy resources become increasingly depleted and ecological environments deteriorate, the global community faces escalating energy crises and environmental challenges.[1,2] In this context, hydrogen energy has emerged as a strategic option for global energy transition due to its high energy conversion efficiency (>60% in PEM electrolyzers), zero-carbon emissions, and infinite renewability.[3,4] Water electrolysis, a promising hydrogen production method, involves two critical electrochemical reactions: the oxygen evolution reaction (OER) at the anode and the hydrogen evolution reaction (HER) at the cathode.[5,6] While HER follows a two-electron transfer process, the OER entails four consecutive proton-coupled electron transfer steps with dynamic intermediate states, resulting in inherently sluggish kinetics that require overpotentials exceeding 300 mV (vs RHE) even for state-of-the-art RuO_2 catalysts.[7,8] Noble metal catalysts exhibit exceptional activity but suffer from prohibitively high costs and limited natural reserves, hindering large-scale deployment.[9,10] On the other hand, freshwater represents only a small fraction of the water resources, while seawater dominates, making seawater electrolysis an appealing area of research.[11,12] The abundant chloride ions present in natural seawater undergo oxidation reactions at the anode, which kinetically suppresses the OER.[13] To prevent hypochlorite formation, OER catalysts must achieve high current density output at overpotentials below 480 mV.[14,15]

Prussian blue analogs (PBAs), which possess open-framework structures enabling reversible intercalation/deintercalation of alkali metal ions, contain abundant transition metals within their frameworks.[16,17] These structural and compositional features make PBAs suitable candidates for both the OER and HER catalysis. Muthurasu et al. successfully incorporated Fe into Ni_2P through a phosphidation technique on nickel foam. Density functional theory (DFT) calculations revealed that Fe doping elevated the d-band center energy level of Ni_2P, thereby enhancing adsorption capabilities for OER and HER intermediates, while improving the conductivity and active site availability.[18] Tarigan et al. demonstrated that dual-

Received: July 21, 2025
Revised: October 4, 2025
Accepted: November 5, 2025
Published: November 17, 2025

https://doi.org/10.1021/acsami.5c14223
ACS Appl. Mater. Interfaces 2025, 17, 64340−64353

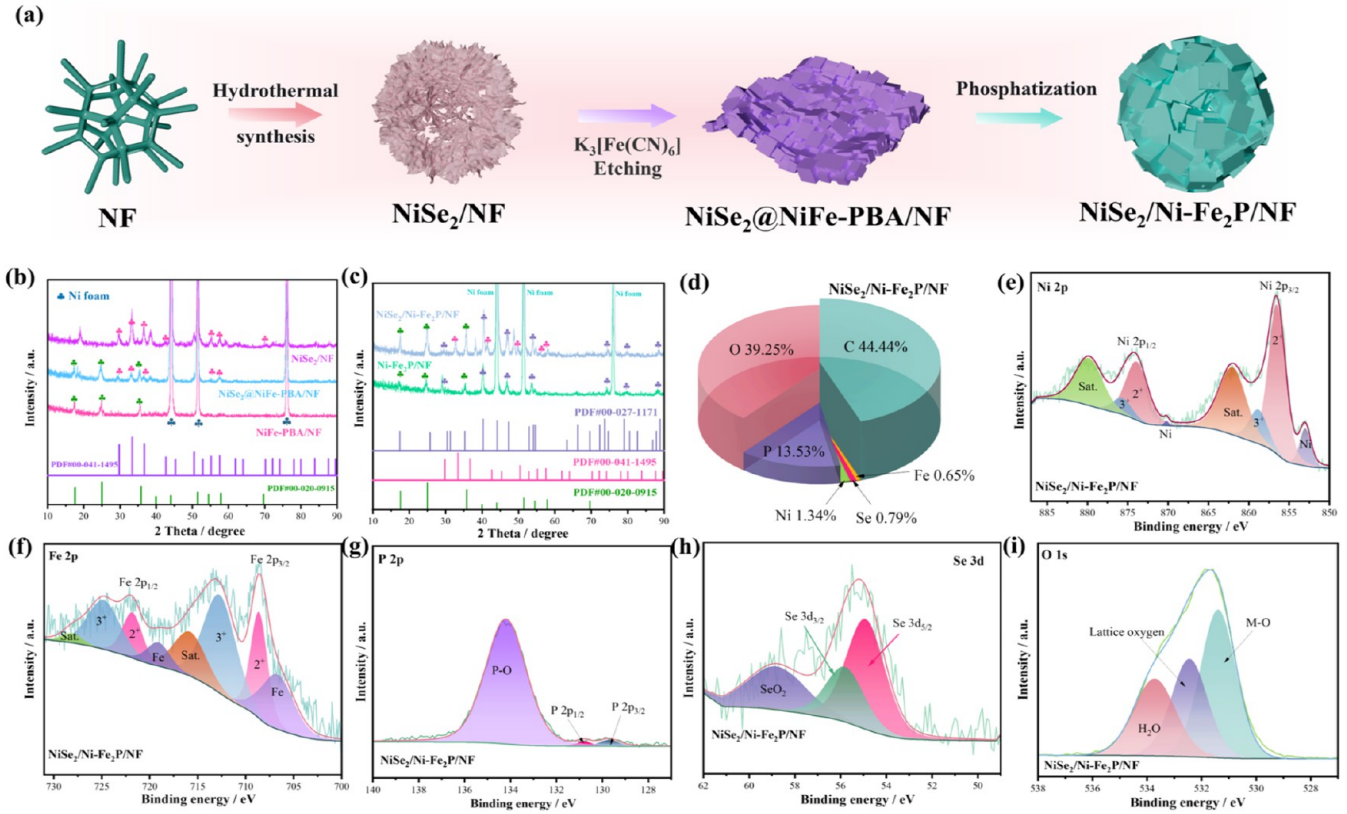

Figure 1. (a) Synthetic illustration of spherical $NiSe_2$/Ni−Fe_2P/NF samples. (b) XRD patterns of $NiSe_2$/NF, NiFe-PBA/NF, and $NiSe_2$@NiFe-PBA/NF. (c) XRD patterns of $NiSe_2$/Ni−Fe_2P/NF and Ni−Fe_2P/NF. (d) XPS spectra of elemental composition for $NiSe_2$/Ni−Fe_2P/NF. XPS of (e) Ni 2p, (f) Fe 2p, (g) P 2p, (h) Se 3d, and (i) O 1s for $NiSe_2$/Ni−Fe_2P/NF.

driven reconstruction through graphene quantum dot (GQD) modification and UV/ozone treatment effectively modulated the electronic structure of CoFe PBA. It enables the CoFe PBA/GQD-UV catalyst to reach 77 mV overpotential.[19] Zhang et al. successfully synthesized hollow Co−Fe PBA structures through precise morphological control of PBAs. Subsequent phosphidation treatment resulted in porous hollow nanobox structures composed of CoP-FeP, which achieved a current density of 10 mA cm^{-2} at an overpotential of 230 mV.[20] However, the performance of the above catalysts still does not meet the requirements for commercialization. The catalytic activity of PBAs can be effectively enhanced through strategies, such as doping, heterostructure construction, and other modification approaches.

In this study, $NiSe_2$ nanosheets were employed as self-sacrificing templates to construct $NiSe_2$@NiFe-PBA nanoboxes through the strong etching capability of $K_3[Fe(CN)_6]$. Subsequently, a phosphidation treatment produced $NiSe_2$/Ni−Fe_2P heterostructures with unique nanocubic spherical morphologies, where the nanoboxes assembled into spherical configurations to increase reaction contact areas and expose more active sites. This performance advantage originated from the surface reconstruction process during which intrinsic active species such as NiOOH and FeOOH formed in situ following directional leaching of P elements. Consequently, the $NiSe_2$/Ni−Fe_2P sample exhibited excellent OER catalytic activity, requiring only 263 and 281 mV to achieve 100 mA cm^{-2} current density in 1.0 M KOH and alkaline seawater environments, respectively. Furthermore, systematic evaluation of HER performance across all samples demonstrated that the $NiSe_2$@NiFe-PBA/NF composite required only 168 mV overpotential to attain a −10 mA cm^{-2} current density in 1.0 M KOH electrolyte, showcasing superior HER catalytic activity. DFT calculations revealed that compared with pure $NiSe_2$, the $NiSe_2$@NiFe-PBA heterostructure exhibited significantly enhanced electronic density of states near the Fermi level and improved charge transfer capabilities at the interface, thereby contributing to its exceptional catalytic performance.

2. METHODS

2.1. Preparation of Materials. *2.1.1. Synthesis of $Ni(OH)_2$ Precursor.* Initially, nickel foam substrates were pretreated by immersing 5 × 5 cm square-shaped nickel foam samples into a 3 M HCl solution, followed by ultrasonication for 15−20 min to remove surface oxides. Subsequently, the samples were transferred to deionized water and further cleaned by ultrasonication for 15−20 min. This two-step sequential treatment yielded pretreated nickel foam substrates.

For the hydrothermal synthesis of $Ni(OH)_2$ precursor, 2 mM $Ni(NO_3)_2{\cdot}6H_2O$, 3 mM NH_4F, and 8 mM urea were dissolved in 60 mL of deionized water under magnetic stirring at room temperature for 20 min to obtain a homogeneous precursor solution. The cleaned nickel foam substrates and the precursor solution were transferred to a 100 mL autoclave and heated at 120 °C for 6 h. After natural cooling to room temperature, the as-prepared samples were washed with deionized water and ethanol, respectively. Finally, the samples were dried in an oven at 60 °C for 12 h, resulting in $Ni(OH)_2$ precursor-loaded nickel foam substrates.

2.1.2. Preparation of $NiSe_2$ Electrocatalyst. For the hydrothermal synthesis of $NiSe_2$ electrocatalyst, 2.8 g of NaOH and 0.1 g of selenium powder were dissolved in 50 mL of deionized water under magnetic stirring at room temperature for 1 h to form a homogeneous solution. The solution was transferred to a 100 mL autoclave and

https://doi.org/10.1021/acsami.5c14223
ACS Appl. Mater. Interfaces 2025, 17, 64340−64353

heated at 200 °C for 13 h. After natural cooling to room temperature, the previously obtained $Ni(OH)_2$ precursor was immersed in the reaction solution and further hydrothermally treated at 180 °C for 1 h. The resulting samples were washed with deionized water and ethanol, followed by drying at 60 °C for 12 h to produce the $NiSe_2$/NF electrocatalyst.

2.1.3. Preparation of $NiSe_2$@NiFe-PBA/NF Electrocatalyst. For the hydrothermal synthesis of $NiSe_2$@NiFe-PBA/NF electrocatalyst, 0.6 mM $K_3[Fe(CN)_6]$ was dissolved in 60 mL of deionized water under magnetic stirring at room temperature to form a homogeneous solution. The $NiSe_2$/NF samples and the solution were transferred to a 100 mL autoclave and heated to 90 °C for 24 h. After being naturally cooled to room temperature, the products were washed with deionized water and ethanol, respectively, followed by drying at 60 °C for 12 h, yielding the $NiSe_2$@NiFe-PBA/NF electrocatalyst.

2.1.4. Preparation of $NiSe_2$/Ni−Fe_2P/NF Electrocatalyst. For the vapor-phase phosphidation of $NiSe_2$/Ni−Fe_2P/NF electrocatalyst, 1 g of NaH_2PO_2 was placed upstream in a quartz tube as a phosphorus source, while the $NiSe_2$@NiFe-PBA/NF sample was vertically positioned downstream. After three cycles of vacuum-purging with argon, phosphidation was conducted under a high-purity argon atmosphere (99.999%) at a heating rate of 2 °C/min to 350 °C, followed by isothermal treatment for 120 min. The product was naturally cooled to room temperature, resulting in the $NiSe_2$/Ni−Fe_2P/NF electrocatalyst.

2.1.5. Preparation of Ni−Fe_2P/NF Electrocatalyst. This process was identical to Sections 2.1.3 and 2.1.4, with the exception that the $Ni(OH)_2$ precursor was substituted for $NiSe_2$/NF.

2.2. Electrocatalytic Performance Evaluation. All electrocatalytic performances were measured by using an IviumSoft electrochemical workstation. OER and HER tests were conducted in a three-electrode system with the as-prepared electrocatalysts as working electrodes and Hg/HgO as the reference electrode. Graphite rods and platinum sheets were used as counter electrodes for HER and OER, respectively, with scan rates of 5 and 2 mV s^{-1}. The electrolytes consisted of 1 M KOH (pH = 13.7) and 1 M KOH + seawater (pH = 13.51) solution. Both HER and OER potentials were converted to the reversible hydrogen electrode (RHE) scale using the equation: E (vs RHE) = E (vs Hg/HgO) + 0.059 × pH + 0.098 V. Additionally, overall water-splitting performance was evaluated in a two-electrode configuration with a scan rate of 5 mV s^{-1}.

2.3. Material Characterization. The phase composition of the materials was analyzed by X-ray diffraction (XRD) on a Rigaku D/max-2500/PC diffractometer using Cu Kα radiation (λ = 1.5406 A). The instrument was operated at 40 kV and 100 mA, and the patterns were collected from 10 to 90° with a step size of 0.02°.

The morphology and microstructure of the materials were observed by using a field-emission scanning electron microscope (SEM, Zeiss Gemini 300) and a transmission electron microscope (TEM, JEM-2100 PLUS).

The surface elemental composition and chemical states were analyzed by X-ray photoelectron spectroscopy (XPS, ESCALAB250, Al Kα sources).

2.4. Theoretical Calculation. First-principles DFT calculations were performed using the Vienna Ab initio Simulation Package (VASP), where electron interactions were described through the generalized gradient approximation (GGA) combined with PBE pseudopotentials. A plane-wave cutoff energy of 300 eV was applied for all calculations. The crystal structures were fully optimized until the forces on all atoms were below 0.05 eV/Å, with the energy convergence criteria set to 10^{-5} eV/atom. The (210) crystal plane of $NiSe_2$ was first modeled, followed by the (220) crystal plane of $K_2FeNi(CN)_6$, to construct the $NiSe_2$@NiFe-PBA heterostructure. Based on this, a $NiSe_2$/Ni−Fe_2P heterojunction interface was further constructed using the (210) plane of $NiSe_2$ and the (110) plane of Fe_2P. Simultaneously, partial Ni atoms were doped into the Fe_2P lattice.

3. RESULTS AND DISCUSSION

As illustrated in Figure 1a, the $NiSe_2$/Ni−Fe_2P/NF nanocubic spheres were constructed through a self-sacrificing template strategy combined with vapor-phase phosphidation engineering. First, a three-dimensional $NiSe_2$/NF nanoflower architecture was synthesized via a simple hydrothermal method on nickel foam. Subsequently, $NiSe_2$/NF served as a self-sacrificing template for direct hydrothermal etching with $K_3[Fe(CN)_6]$, inducing the in situ formation of NiFe-PBA on the $NiSe_2$/NF surface. Finally, the $NiSe_2$/Ni−Fe_2P/NF nanocubic spheres were successfully fabricated through a vapor-phase phosphidation treatment, exhibiting both inherent catalytic activity and morphological advantages. X-ray diffraction (XRD) analysis was performed to characterize the crystal structure and phase composition of the synthesized samples. As shown in Figure 1b, diffraction peaks at 2θ = 44.32°, 51.64°, and 76.18° were indexed to the (111), (200), and (220) crystal planes of the nickel foam substrate (JCPDS No. 04-0850). The characteristic peaks at 2θ = 17.52°, 25.00°, and 35.76° corresponded to the (200), (220), and (400) crystal planes of $K_2FeNi(CN)_6$ (JCPDS No. 20-0915), confirming the successful synthesis of the NiFe-PBA/NF sample. For the $NiSe_2$/NF sample, diffraction peaks at 2θ = 29.80°, 33.30°, 36.66°, 42.58°, 55.38°, 57.58°, and 70.32° matched the (200), (210), (211), (220), (321), (420), and (421) crystal planes of $NiSe_2$/NF (JCPDS No. 41-1495), indicating excellent crystallinity. Notably, the XRD pattern of the $NiSe_2$/NiFe-PBA/NF composite sample preserved the characteristic peaks of $NiSe_2$/NF while fully displaying the diffraction features of NiFe-PBA/NF, demonstrating the successful integration of both components. After vapor-phase phosphidation treatment (Figure 1c), new diffraction peaks emerged at 2θ = 29.48°, 40.46°, 47.24°, 54.08°, 74.52°, and 79.88°, which were assigned to the (110), (111), (210), (300), (400), and (401) crystal planes of the Fe_2P phase (JCPDS No. 27-1171). The amorphous peak at 2θ = 88.78° also belonged to the Fe_2P phase, confirming the formation of Fe_2P during phosphidation in the $NiSe_2$/Ni−Fe_2P/NF sample. Importantly, the Ni−Fe_2P/NF sample differed from $NiSe_2$/Ni−Fe_2P/NF as no characteristic peaks of $NiSe_2$/NF were detected in the former.

To gain deeper insights into the electronic structure evolution, X-ray photoelectron spectroscopy (XPS) analysis was systematically conducted to characterize the surface chemical states of the $NiSe_2$/Ni−Fe_2P/NF catalyst. As shown in Figure 1d, elemental relative content mapping revealed the presence of Ni, Fe, P, Se, and O in the $NiSe_2$/Ni−Fe_2P/NF sample. The Ni 2p XPS spectrum (Figure 1e) exhibited peaks at 853.0 and 870.20 eV corresponding to Ni^0 from the NF substrate.[21] Two distinct peaks at 856.5 and 873.9 eV were assigned to Ni^{2+} $2p_{3/2}$ and Ni^{2+} $2p_{1/2}$, while peaks at 858.8 and 875.7 eV originated from Ni^{3+} $2p_{3/2}$ and Ni^{3+} $2p_{1/2}$.[22] The satellite peaks at 862.0 and 879.8 eV further confirmed the coexistence of Ni^{2+} and Ni^{3+} species in the $NiSe_2$/Ni−Fe_2P/NF sample.[23] The Fe 2p XPS spectrum (Figure 1f) showed peaks at 706.7 and 719.1 eV assigned to Fe^0, indicating residual metallic Fe from incomplete reaction during the etching process.[24] In the Fe $2p_{3/2}$ region, the binding energy at 708.6 eV corresponded to Fe^{2+}, while the peak at 712.7 eV was attributed to Fe^{3+}.[25] Similarly, Fe $2p_{1/2}$ signals at 721.8 eV (Fe^{2+}) and 724.8 eV (Fe^{3+}) were observed, with satellite peaks at 715.8 and 728.1 eV, confirming dual

https://doi.org/10.1021/acsami.5c14223
ACS Appl. Mater. Interfaces 2025, 17, 64340−64353

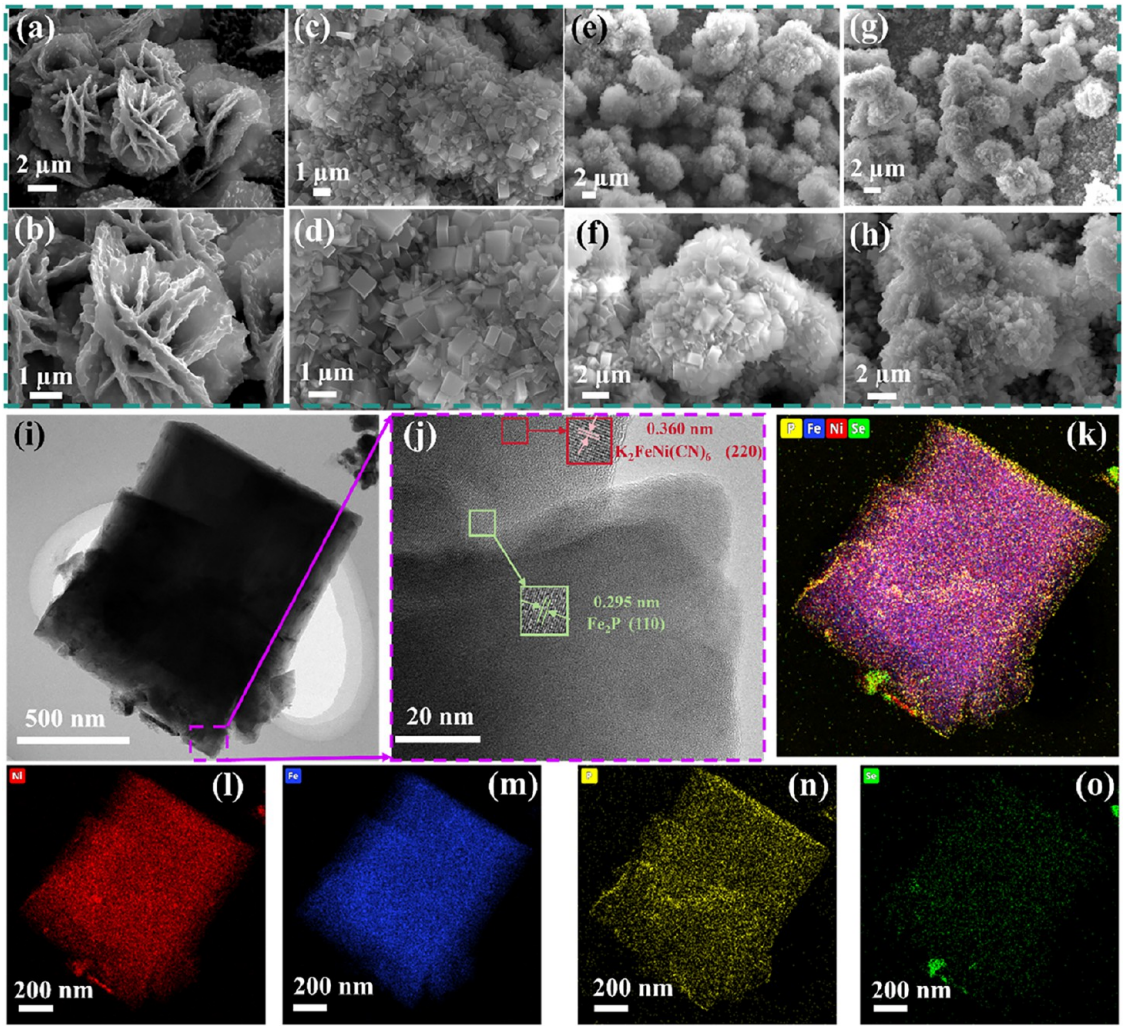

Figure 2. SEM images of (a, b) $NiSe_2$/NF, (c, d) $NiSe_2$@NiFe-PBA/NF, (e, f) $NiSe_2$/Ni−Fe_2P/NF, and (g, h) Ni−Fe_2P/NF. (i, j) TEM and HRTEM images of $NiSe_2$/Ni−Fe_2P/NF samples. (k−o) EDS mapping of $NiSe_2$/Ni−Fe_2P/NF samples.

oxidation states of Fe in the sample.[26] In the P 2p XPS spectrum (Figure 1g), the peaks at 129.7 and 130.8 eV were attributed to the P $2p_{3/2}$ and $2p_{1/2}$ regions of Fe−P bonds, while the peak at 134.2 eV corresponded to P−O bonding.[27] The Se 3d spectrum (Figure 1h) displayed binding energies at 54.9 and 55.8 eV for Se $3d_{5/2}$ and $3d_{3/2}$, respectively.[28] A broad peak at 58.8 eV indicated the presence of SeO_2 species.[29] For the O 1s spectrum (Figure 1i), the binding energies at 531.39, 532.44, and 533.72 eV were assigned to metal−oxygen bonds, lattice oxygen, and adsorbed H_2O species, respectively.[30] These systematic XPS analyses provided direct evidence of the complex surface chemical states and electronic interactions within the $NiSe_2$/Ni−Fe_2P/NF heterostructure.

The morphological characteristics of all samples were investigated by scanning electron microscopy (SEM). Figure S1 displays the SEM image of the $Ni(OH)_2$/NF sample, revealing a three-dimensional (3D) nanoflower structure composed of stacked nanosheets. After the hydrothermal selenization treatment (Figure 2a,b), the nanosheet surfaces developed wrinkles, forming a $NiSe_2$ nanoflower architecture constructed from interlaced wrinkled nanosheets. This unique structure significantly increases the contact area, thereby enhancing the sample's catalytic performance. Figure 2c,d displays SEM micrographs of $NiSe_2$@NiFe-PBA/NF at varying magnifications, showing regular cubic PBAs nanobox structures that formed in situ on the surface after the $K_3[Fe(CN)_6]$-mediated interfacial redox reaction. These nanoboxes are uniformly anchored onto the nickel foam framework with their well-defined morphology and ordered arrangement, confirming the effectiveness of the controlled synthesis strategy employing $NiSe_2$/NF as a partial sacrificial template. Figure 2e,f illustrates SEM images of $NiSe_2$/Ni−Fe_2P/NF at different magnifications, demonstrating significant aggregation of originally discrete nanoboxes following vapor-phase phosphidation treatment. This process ultimately produced irregular nanocubic spheres assembled from multiple aggregated nanocubes. Figure 2g,h shows SEM observations of Ni−Fe_2P/NF at varying magnifications, which exhibit morphological similarities to $NiSe_2$/Ni−Fe_2P/NF. However, the Ni−Fe_2P/NF sample displays substantially reduced nanocubic sphere density on the nickel foam surface, with smaller and unevenly distributed nanoboxes attached to the sphere surfaces compared to the $NiSe_2$/Ni−Fe_2P/NF counterpart.

Transmission electron microscopy (TEM) was employed to further characterize the microstructural features of the materials. As shown in Figure 2i, the cubic PBA nanobox morphology was clearly observed in the $NiSe_2$/Ni−Fe_2P/NF composite. After the vapor-phase phosphidation treatment, the

https://doi.org/10.1021/acsami.5c14223
ACS Appl. Mater. Interfaces 2025, 17, 64340−64353

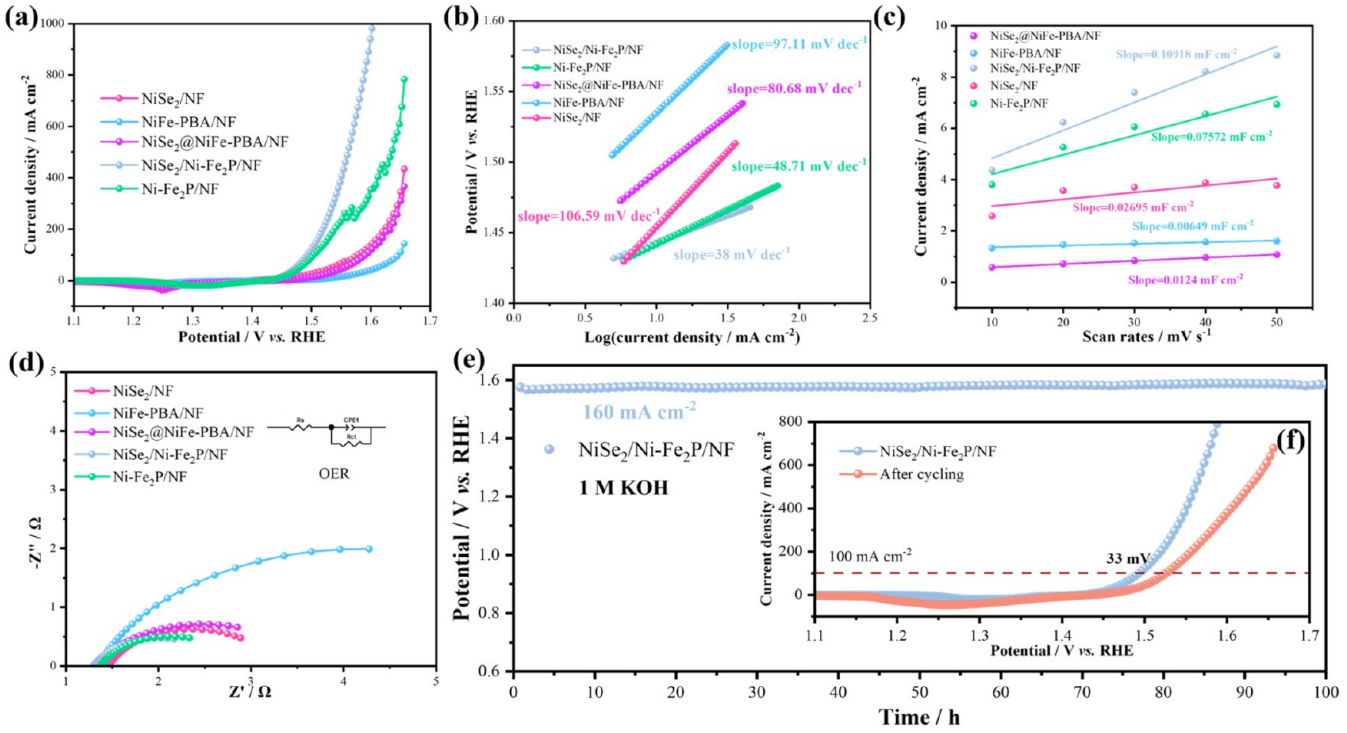

Figure 3. OER performances of the electrocatalysts in 1.0 M KOH. (a) LSV curves. (b)Tafel plots. (c) Double-layer capacitance. (d) Nyquist plots. (e) Cycle Stability. (f) LSV curves of the initial and after cycling for 100 h.

nanobox surfaces exhibited significant roughening, which originated from surface reconstruction during Fe_2P phase formation. As shown in Figure 2j, the measured lattice fringe spacings were 0.360 and 0.295 nm, corresponding to the (220) crystal plane of $K_2FeNi(CN)_6$ and the (110) crystal plane of Fe_2P, respectively, which confirms the coexistence of PBA precursors and phosphidation products within the composite material. Figure S2a,b presents the TEM images of the $NiSe_2$/NF sample, revealing that $NiSe_2$ adopts a wrinkled nanosheet morphology. As shown in Figure S2b, distinct lattice fringes are observed with an interplanar spacing of 0.211 nm corresponding to the (220) plane of $NiSe_2$. Combined with energy-dispersive X-ray spectroscopy (EDS) mapping (Figure S3), which confirms the presence of Ni and Se in the sample, these observations provide strong evidence for the successful synthesis of $NiSe_2$. In contrast, no lattice fringes of $NiSe_2$ could be identified in the $NiSe_2$/Ni−Fe_2P/NF sample. This is attributed to the formation of $K_2FeNi(CN)_6$ crystals during the potassium ferricyanide etching process. These crystals deposit on the material surface, and their lattice structure masks the lattice information on $NiSe_2$, preventing clear identification. The EDS mapping (Figure 2k−o) revealed uniform spatial distributions of Ni, Fe, Se, and P elements within individual $NiSe_2$/Ni−Fe_2P/NF samples. The coexistence of Ni and Fe reflects the stability of the nanocubic framework, while the synergistic distribution of Se and P confirms the successful transformation of the $NiSe_2$ template during the phosphidation process.

To evaluate the OER performance of the prepared samples in 1 M KOH, Figure 3a presents the linear sweep voltammetry (LSV) curves for all samples. Among the tested materials, the $NiSe_2$/Ni−Fe_2P/NF sample exhibited superior OER activity, delivering an overpotential of 213 mV at 10 mA cm^{-2} current density. At 100 mA cm^{-2}, this sample required only 263 mV, which was 84 mV lower than $NiSe_2$/NF, 153 mV lower than NiFe-PBA/NF, 98 mV lower than $NiSe_2$@NiFe-PBA/NF, and 11 mV lower than Ni−Fe_2P/NF. As shown in the overpotential plot of Figure S4, the $NiSe_2$/Ni−Fe_2P/NF sample exhibits superior OER performance in 1.0 M KOH compared to other samples. Further kinetic analysis through Tafel slope measurements (Figure 3b) revealed that the $NiSe_2$/Ni−Fe_2P/NF sample achieved the smallest slope value of 38 mV dec^{-1}, significantly outperforming $NiSe_2$/NF (106.59 mV dec^{-1}), NiFe-PBA/NF (97.11 mV dec^{-1}), $NiSe_2$@NiFe-PBA/NF (80.68 mV dec^{-1}), and Ni−Fe_2P/NF (48.71 mV dec^{-1}), confirming its accelerated charge transfer process and enhanced reaction kinetics. Combined with electrochemical double-layer capacitance (C_{dl}) testing (Figure 3c), the $NiSe_2$/Ni−Fe_2P/NF sample demonstrated a C_{dl} value of 0.10918 mF cm^{-2}, surpassing all comparative samples and indicating an abundant active site distribution. Electrochemical impedance spectroscopy (EIS) analysis (Figure 3d) further indicated that $NiSe_2$/Ni−Fe_2P/NF exhibits a smaller charge transfer resistance (R_{ct} = 1.43 Ω), confirming its superior charge transfer kinetics and effectively suppressing diffusion limitations. Chronopotentiometric stability tests (Figure 3e) demonstrated that the $NiSe_2$/Ni−Fe_2P/NF sample maintained stable catalytic performance after 100 h of continuous operation at a current density of 160 mA cm^{-2}. As shown in Figure 3f, the overpotential at 100 mA cm^{-2} decreased by only 33 mV between the LSV curves recorded before and after cycling, indicating that the sample possesses good structural stability and sustained catalytic activity in alkaline electrolyte environments.

To further investigate the electrochemical performance of $NiSe_2$/NF and $NiSe_2$/Ni−Fe_2P/NF samples, Bode plots and DRT diagrams were analyzed across a potential range of 10−150 mA cm^{-2}, relative to the RHE. As shown in Figure 4a, the

https://doi.org/10.1021/acsami.5c14223
ACS Appl. Mater. Interfaces 2025, 17, 64340−64353

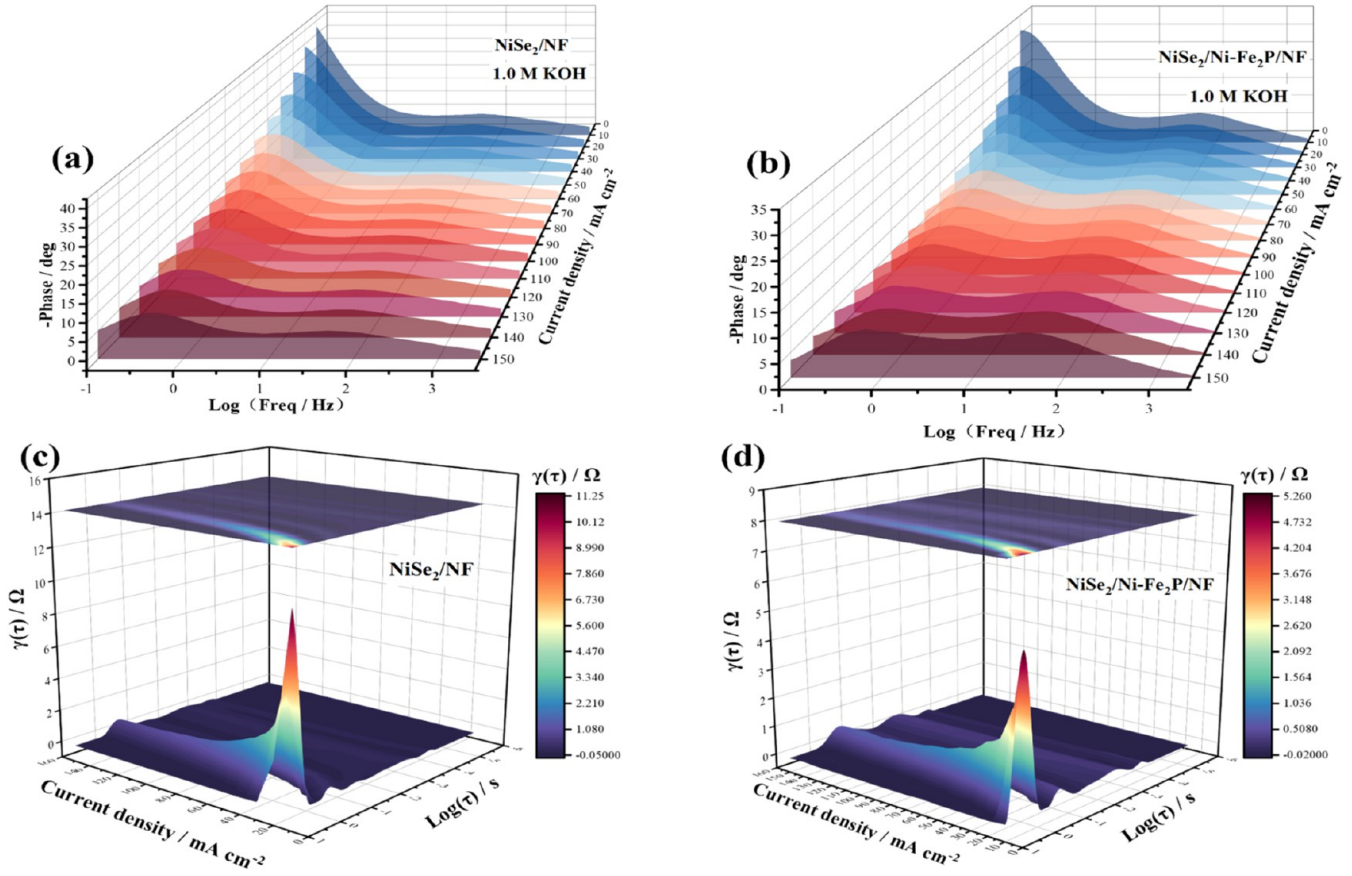

Figure 4. Electrochemical impedance characterization of catalysts in 1.0 M KOH. Bode plots of (a) $NiSe_2$/NF and (b) $NiSe_2$/Ni−Fe_2P/NF. DRT plots of (c) $NiSe_2$/NF and (d) $NiSe_2$/Ni−Fe_2P/NF.

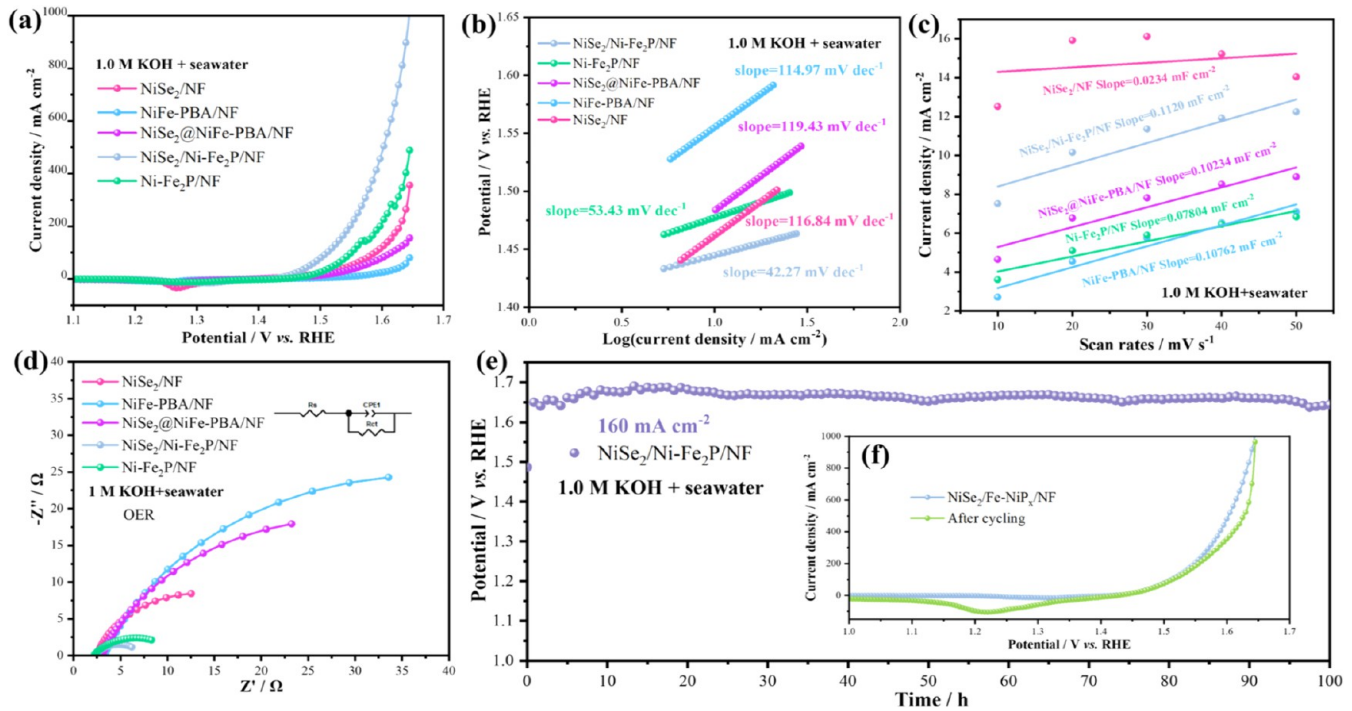

Figure 5. OER performances of the electrocatalysts in 1.0 M KOH + seawater. (a) LSV curves. (b) Tafel plots. (c) Double-layer capacitance. (d) Nyquist plots. (e) Cycle Stability. (f) LSV curves.

Bode plot of $NiSe_2$/NF indicates that the phase angle initially increases and subsequently decreases with increasing frequency, exhibiting a narrow overall phase angle range and pronounced diffusion suppression in the low-frequency

https://doi.org/10.1021/acsami.5c14223
ACS Appl. Mater. Interfaces 2025, 17, 64340−64353

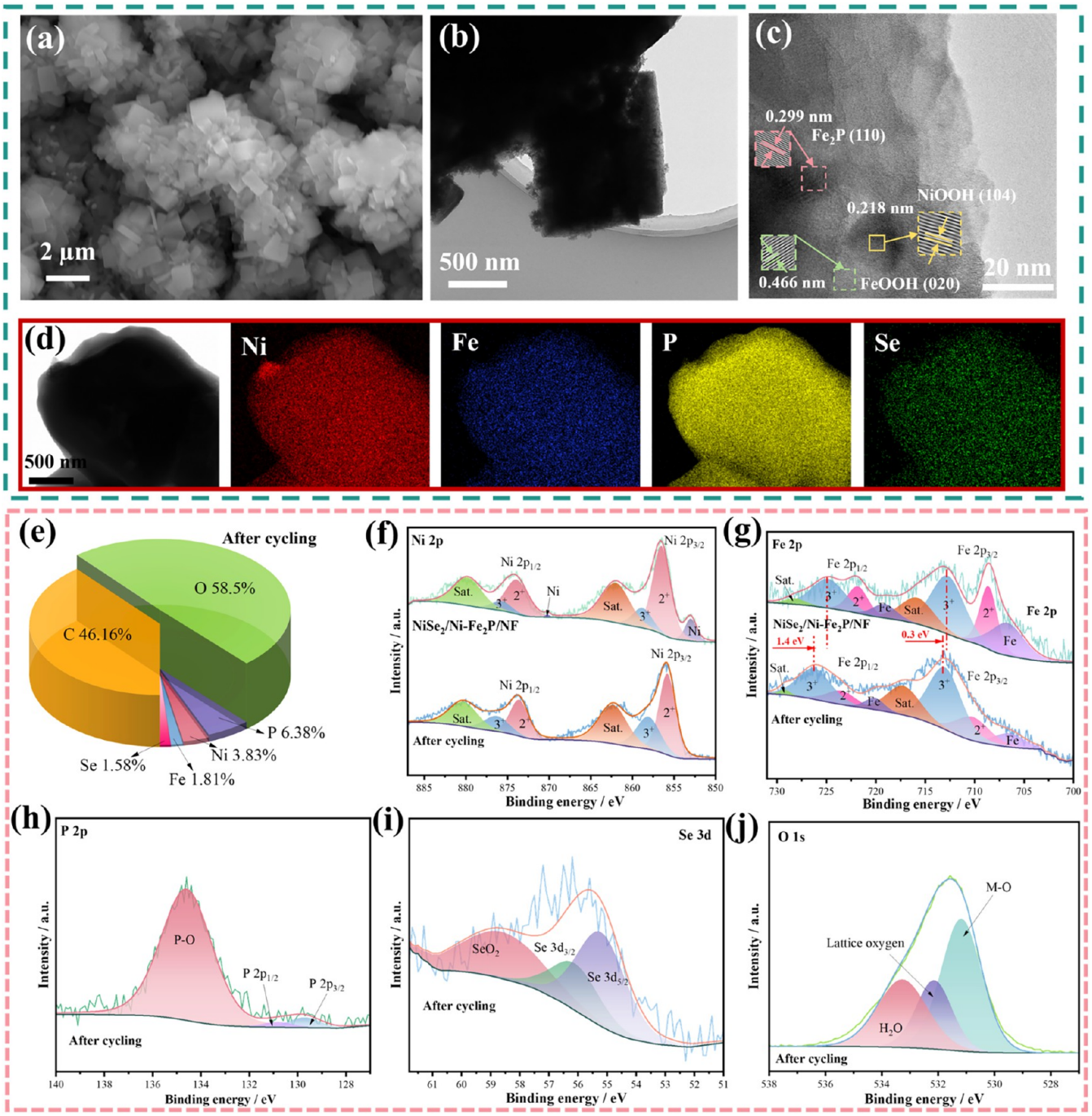

Figure 6. Structure characterization of the $NiSe_2$/Ni−Fe_2P/NF catalysts after cycling for OER. (a) SEM images. (b) TEM images. (c) HRTEM images. (d) EDS mapping. (e) XPS spectra of elemental composition. XPS of (f) Ni 2p, (g) Fe 2p, (h) P 2p, (i) Se 3d, and (j) O 1s.

region.[31] In comparison, the Bode plot of $NiSe_2$/Ni−Fe_2P/NF (Figure 4b) follows a similar phase angle trend but demonstrates a broader phase angle range and reduced diffusion suppression at low frequencies. This observation suggests that the charge transfer kinetics at the heterointerface are significantly optimized, enhancing interfacial electron migration rates and alleviating diffusion limitations. Figure 4c reveals that $NiSe_2$/NF exhibits a wide $\gamma(\tau)$ range (−0.05 to 11.25 Ω) with a prominent peak at $\tau \approx 1$ s, indicating substantial charge transfer resistance that compromises catalytic performance. In contrast, the introduction of the heterostructure (Figure 4d) narrows the $\gamma(\tau)$ range to −0.02 to 5.26 Ω, reduces peak intensity, and centralizes the distribution. These changes enhance charge transfer efficiency and reduce interfacial impedance, thereby improving catalytic performance.[32,33] The combined analysis of Bode plots and DRT diagrams demonstrates that constructing a Ni−Fe_2P heterointerface using $NiSe_2$ as a sacrificial template significantly enhances the catalytic activity and stability through interfacial effects.

The evaluation of $NiSe_2$/Ni−Fe_2P/NF in an alkaline electrolyte demonstrated its exceptional OER performance. Building on this, we further assessed its OER activity in an alkaline seawater electrolyte (1.0 M KOH + seawater). As shown in the LSV curves (Figure 5a) and the overpotential plot (Figure S5), the $NiSe_2$/Ni−Fe_2P/NF nanospheres

https://doi.org/10.1021/acsami.5c14223
ACS Appl. Mater. Interfaces 2025, 17, 64340−64353

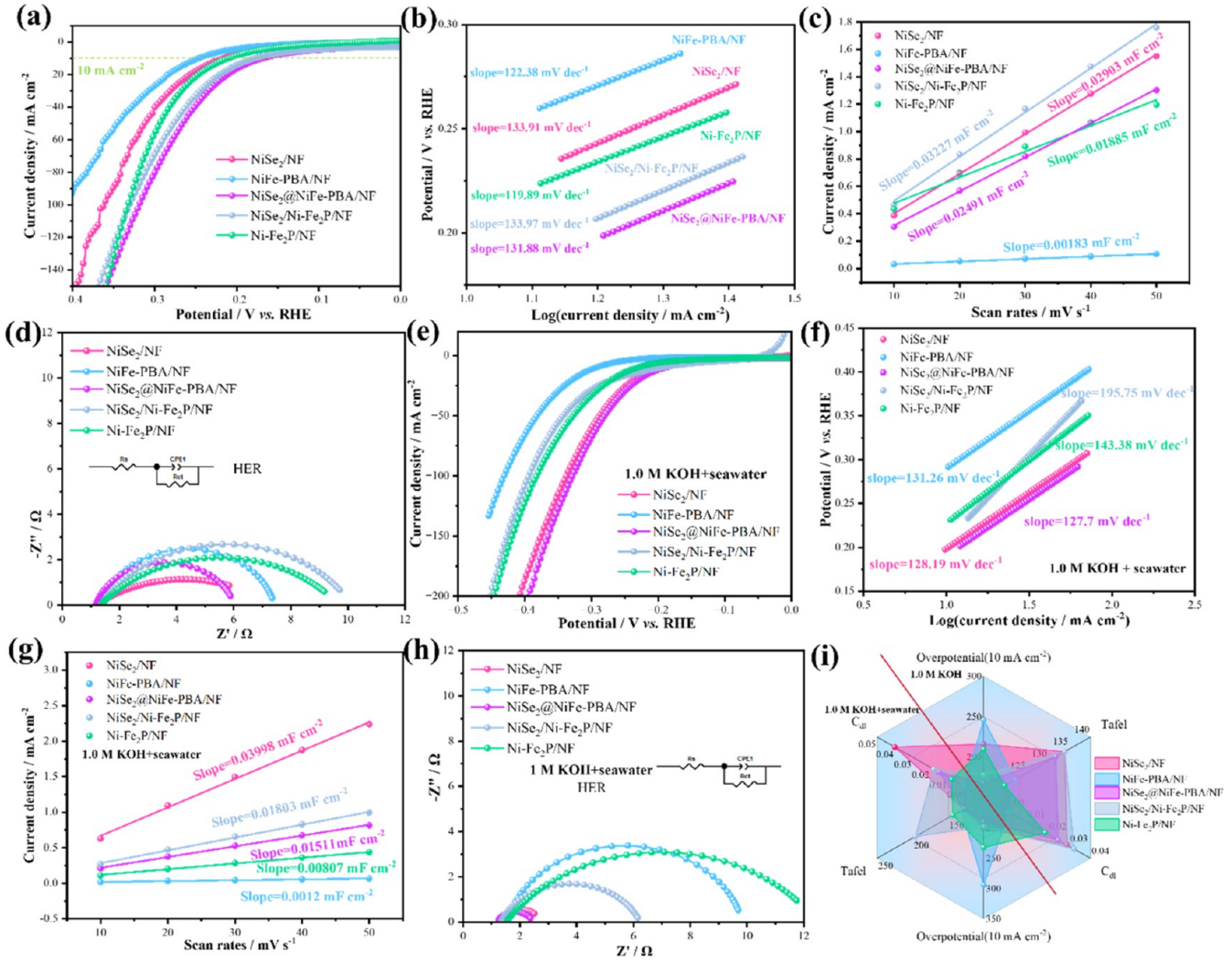

Figure 7. HER performances of the electrocatalysts in 1.0 M KOH. (a) LSV curves. (b) Tafel plots. (c) Double-layer capacitance. (d) Nyquist plots. HER performances of the electrocatalysts in 1.0 M KOH + seawater. (e) LSV curves. (f) Tafel plots. (g) Double-layer capacitance. (h) Nyquist plots. (i) Radar chart.

retained outstanding OER catalytic activity, requiring overpotentials of only 214 and 281 mV to achieve current densities of 10 and 100 mA cm^{-2}, respectively. In contrast, the $NiSe_2$@NiFe-PBA/NF and Ni−Fe_2P/NF samples required 382 and 321 mV, respectively, to reach 100 mA cm^{-2}, indicating significantly inferior catalytic performance. The oxygen evolution kinetics in alkaline seawater were analyzed through Tafel slope measurements. As illustrated in Figure 5b, compared with the 1 M KOH electrolyte, all samples exhibited slower OER kinetics in alkaline seawater. The Tafel slopes for $NiSe_2$/NF, NiFe-PBA/NF, $NiSe_2$@NiFe-PBA/NF, $NiSe_2$/Ni−Fe_2P/NF, and Ni−Fe_2P/NF were 116.84, 114.97, 119.43, 42.27, and 53.43 mV dec^{-1}, respectively. Notably, the $NiSe_2$/Ni−Fe_2P/NF sample displayed a Tafel slope significantly lower than that of all other samples, confirming its superior OER catalytic kinetics even in alkaline seawater. To evaluate catalytic activity, electrochemical double-layer capacitance measurements were conducted to determine the ECSA. As shown in Figure 5c, the $NiSe_2$/Ni−Fe_2P/NF sample exhibited an ECSA of 0.1120 mF cm^{-2}, surpassing all comparative samples and indicating higher intrinsic activity. As shown in the EIS plot (Figure 5d), the $NiSe_2$/Ni−Fe_2P/NF catalyst exhibits a smaller charge transfer resistance (R_{ct}), indicating that it achieves the fastest charge transfer kinetics during the OER. Chronopotentiometric tests conducted under constant current conditions for nearly 100 h (Figure 5e) demonstrated that the sample maintained a stable voltage output without significant decay. Furthermore, compared to the LSV curves recorded before cycling (Figure 5f), the overpotential at a current density of 100 mA cm^{-2} changed by only 3 mV, further confirming the sample's exceptional resistance to seawater corrosion and its ability to operate stably under harsh environmental conditions for extended periods. Compared to previously reported catalysts (Table S1), the $NiSe_2$/Ni−Fe_2P/NF sample demonstrates significantly superior OER electrocatalytic performance.

During the OER, the formation of metal (oxy) hydroxides on the catalyst surface and dissolution of original elements may induce morphological and compositional reconstruction.[34] These reconstructed species are often considered as the true active sites for OER.[35] To gain deeper insights into the reconstruction behavior and identify the genuine active sites of $NiSe_2$/Ni−Fe_2P/NF during the OER, systematic characterization and analysis were conducted using SEM, TEM, and XPS to investigate the morphological changes and chemical states after the OER testing. The SEM image in Figure 6a

https://doi.org/10.1021/acsami.5c14223
ACS Appl. Mater. Interfaces 2025, 17, 64340−64353

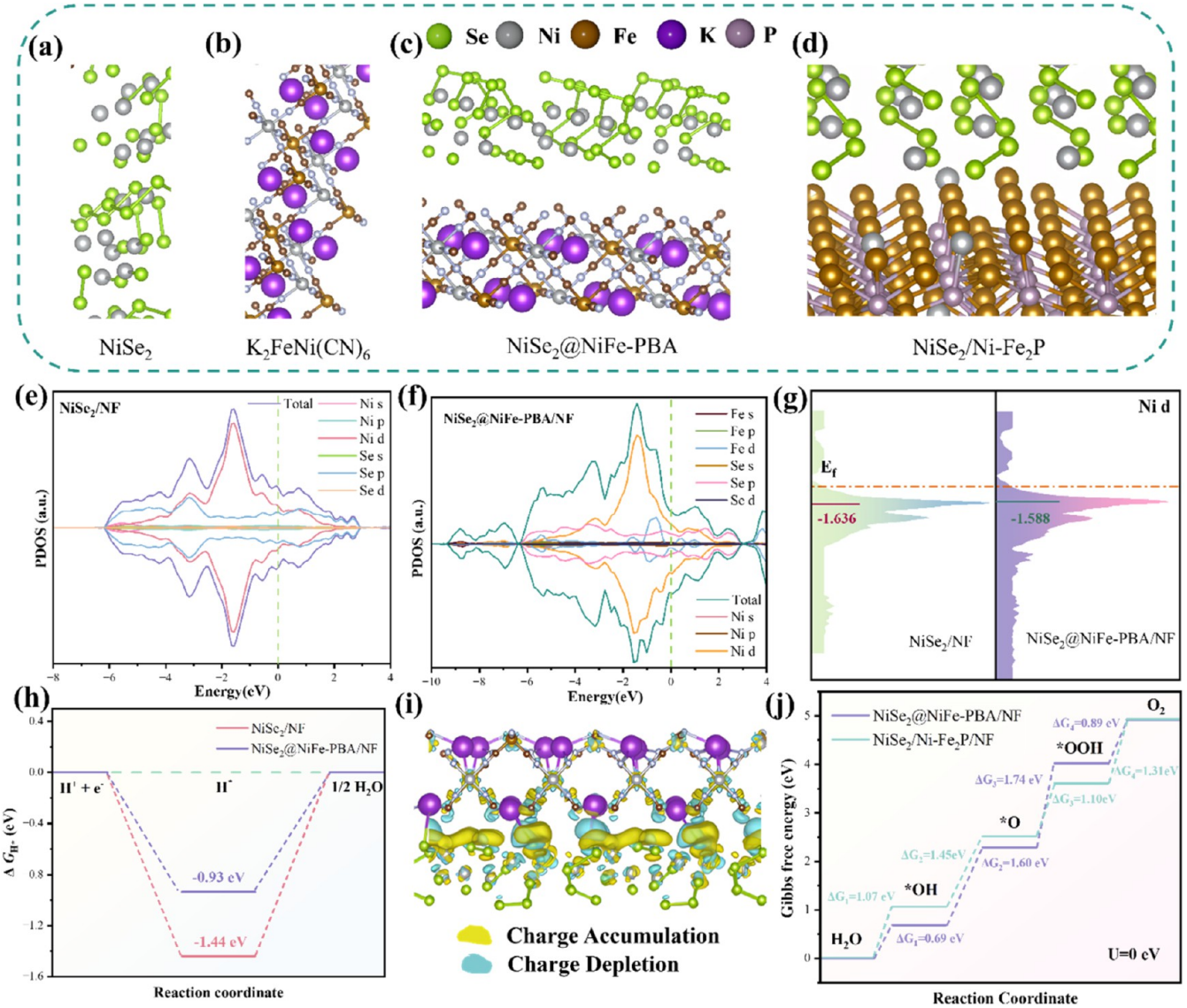

Figure 8. DFT calculation of the samples. Structural models of $NiSe_2$/NF (a), $K_2FeNi(CN)_6$ (b), $NiSe_2$@NiFe-PBA (c), $NiSe_2$/Ni−Fe_2P (d). (e) PDOS of $NiSe_2$/NF. (f) PDOS of $NiSe_2$@NiFe-PBA/NF. (g) The value of d-band center of the two structures. (h) Calculated Gibbs free energy diagram for hydrogen adsorption ($\Delta G_{(H^*)}$) on the surfaces of different models. (i) Electron density difference map of $NiSe_2$@NiFe-PBA/NF, yellow and cyan represent electronic accumulation and depletion, respectively. (j) Calculated free energy diagram of OER (U = 0).

reveals that the original nanocubic structure of $NiSe_2$/Ni−Fe_2P/NF remains well-preserved after prolonged stability testing, but the surface becomes rougher. This observation indicates material reconstruction while further confirming its excellent stability and corrosion resistance. TEM analysis (Figure 6b,c) further reveals that the reconstructed sample exhibits highly disordered lattice fringes composed of numerous low-crystallinity nanoparticles, providing abundant grain boundary structures. As shown in Figure 6c, the observed interplanar spacings of 0.299, 0.466, and 0.218 nm correspond to the (110) plane of Fe_2P (JCPDS No. 27-1171), the (104) plane of NiOOH (JCPDS No. 06-0075), and the (020) plane of FeOOH (JCPDS No. 18-0639), respectively. These results confirm the formation of active species, such as NiOOH and FeOOH, on the surface of $NiSe_2$/Ni−Fe_2P/NF during reconstruction. EDS elemental mapping (Figure 6d) demonstrates uniform distributions of Ni, Fe, P, and Se across the sample.

To further investigate changes in the surface electronic structure, XPS characterization was performed. As shown in Figure 6e, the O content increases significantly after OER testing, while the P content decreases markedly, indicating phosphorus loss during the OER process. The Ni 2p XPS spectrum (Figure 6f) shows weakened signal peaks from the NF substrate, suggesting oxidation of Ni^0 on the surface.[36] In the Fe 2p XPS spectrum (Figure 6g), the intensities of Fe^{2+} peaks decrease, and the Fe^{3+} $2p_{3/2}$ peak shifts 0.3 eV toward higher binding energy, while the Fe^{3+} $2p_{1/2}$ peak shifts 1.4 eV to higher binding energy.[37] This indicates further oxidation of Fe ions to higher valence states on the surface.[38] The P 2p XPS spectrum (Figure 6h) reveals that phosphorus exists primarily as P−O bonds and phosphides (Fe−P), with no significant shift in the P $2p_{3/2}$ and P $2p_{1/2}$ doublet positions, confirming the structural stability of $NiSe_2$/Ni−Fe_2P/NF during OER.[39] The Se 3d XPS spectra (Figure 6i) revealed that the proportion of the SeO_2 peak increased from 28.05% to 35.01% after cycling, indicating partial oxidation of Se during

https://doi.org/10.1021/acsami.5c14223
ACS Appl. Mater. Interfaces 2025, 17, 64340−64353

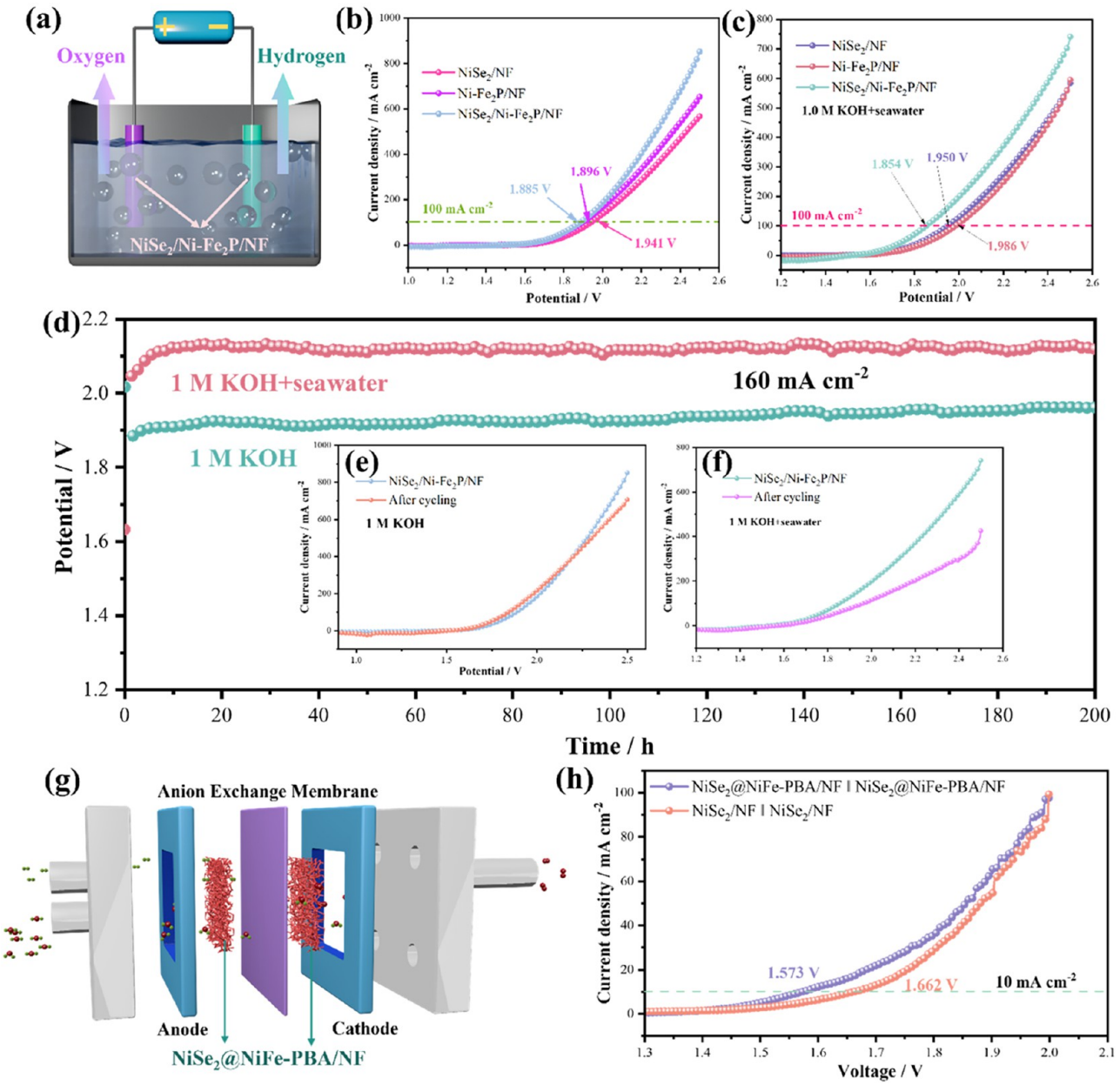

Figure 9. (a) Schematic illustration of overall water splitting. (b) LSV curves of the catalyst in 1 M KOH. (c) LSV curves of the catalyst in 1 M KOH + seawater. (d) Cycling stability of the $NiSe_2$/Ni−Fe_2P/NF sample. (e) LSV curves before and after cycling. (f) LSV curves before and after cycling in 1 M KOH + seawater. (g) Schematic diagram of the AEMWE electrolyzer. (h) Polarization curves of the AEMWE electrolyzer with $NiSe_2$@NiFe-PBA/NF and $NiSe_2$/NF catalysts in 1 M KOH at 25 °C.

the OER process and confirming the occurrence of surface reconstruction.[40] Finally, analysis of the O 1s XPS spectra (Figure 6j) indicated that the total oxygen content on the material surface increased after cycling, with the atomic concentration of M−O bonds rising from 43.6% to 47.8% and the atomic concentration of adsorbed water increasing from 26.8% to 30.1%, further confirming the occurrence of surface reconstruction.[41]

To evaluate the suitability of the prepared samples as bifunctional catalysts, HER testing was conducted on all samples. First, the HER performance was assessed in 1.0 M KOH electrolyte. As shown in the LSV curves (Figure 7a), the $NiSe_2$@NiFe-PBA/NF sample required an overpotential of only 168 mV at −10 mA cm^{-2}, outperforming $NiSe_2$/NF (216 mV), NiFe-PBA/NF (246 mV), $NiSe_2$/Ni−Fe_2P/NF (178 mV), and Ni−Fe_2P/NF (210 mV). To investigate the reaction kinetics, Tafel slopes were calculated from the LSV curves (Figure 7b). Compared to $NiSe_2$/NF (133.91 mV dec^{-1}) and $NiSe_2$/Ni−Fe_2P/NF (133.97 mV dec^{-1}), the $NiSe_2$@NiFe-PBA/NF sample exhibited a lower Tafel slope of 131.88 mV dec^{-1}, indicating faster reaction kinetics. The electrochemical double-layer capacitance (C_{dl}) values (Figure 7c) further revealed that $NiSe_2$@NiFe-PBA/NF displayed higher electrochemical activity (0.02491 mF cm^{-2}), approximately 13 times that of NiFe-PBA/NF (0.00183 mF cm^{-2}). EIS analysis (Figure 7d) demonstrated that $NiSe_2$@NiFe-PBA/NF had a charge transfer resistance (R_{ct}) of 4.85 Ω, lower than that of $NiSe_2$/NF (6.16 Ω), NiFe-PBA/NF (6.01 Ω), $NiSe_2$/Ni−Fe_2P/NF (8.77 Ω), and Ni−Fe_2P/NF (8.35 Ω). Subsequent HER performance testing in alkaline seawater (Figure 7e)

https://doi.org/10.1021/acsami.5c14223
ACS Appl. Mater. Interfaces 2025, 17, 64340−64353

revealed that the $NiSe_2$@NiFe-PBA/NF sample maintained significantly superior catalytic activity at −100 mA cm^{-2} compared with other samples. Based on overpotential measurements, the catalytic activity sequence followed: $NiSe_2$@NiFe-PBA/NF > NiFe-PBA/NF > $NiSe_2$/Ni−Fe_2P/NF > Ni−Fe_2P/NF. As shown in Figure 7f, $NiSe_2$@NiFe-PBA/NF exhibited the lowest Tafel slope (127.70 mV dec^{-1}) in alkaline seawater, further confirming its excellent HER kinetics. Figure 7g highlights that this sample's ECSA was 12.5 times that of NiFe-PBA/NF (0.0012 mF cm^{-2}) and 1.9 times that of Ni−Fe_2P/NF (0.00807 mF cm^{-2}), reinforcing the abundance of surface active sites. EIS analysis (Figure 7h) indicated that the $NiSe_2$@NiFe-PBA/NF heterostructure exhibits the smallest semicircle diameter (R_{ct} = 1.25 Ω), demonstrating faster charge transfer kinetics for this heterostructure. The comprehensive radar chart (Figure 7i) demonstrates that $NiSe_2$@NiFe-PBA/NF delivers an outstanding HER performance in both 1.0 M KOH and alkaline seawater environments. In contrast, although the $NiSe_2$/Ni−Fe_2P/NF sample showed increased electrochemically active surface area after phosphidation treatment, its higher overpotential and reduced overall catalytic performance highlight the advantages of the $NiSe_2$@NiFe-PBA/NF architecture.

Density functional theory (DFT) calculations were performed to elucidate the fundamental reasons for the enhanced electrocatalytic performance. The corresponding models are shown in Figure 8a−d. Comparative analysis of the projected density of states (PDOS) for $NiSe_2$/NF (Figure 8e) and $NiSe_2$@NiFe-PBA/NF (Figure 8f) revealed that the incorporation of NiFe-PBA enhances the atomic density of states nearly close to the Fermi level, thereby increasing the total density of states and improving the conductivity of the catalysts. The position of the d-band center relative to the Fermi energy (E_f) serves as a critical indicator for assessing the interaction strength between adsorbates and the substrate.[42] According to d-band theory (Figure 8g), the d-band centers of $NiSe_2$ and $NiSe_2$@NiFe-PBA relative to E_f are −1.636 eV and −1.588 eV, respectively. This indicates that constructing a heterostructure between $NiSe_2$ and NiFe-PBA shifts the d-band center closer to E_f, thereby strengthening the interaction between adsorbates and the catalyst.[43] To evaluate the origin of the improved HER performance, the hydrogen adsorption energy (ΔG_{H^*}) was analyzed. As shown in Figure 8h, the ΔG_{H^*} values for $NiSe_2$ and $NiSe_2$@NiFe-PBA are −1.44 eV and −0.93 eV, respectively. The latter value is closer to the ideal value of 0 eV, demonstrating that the $NiSe_2$@NiFe-PBA heterostructure optimizes the surface hydrogen adsorption energy and reduces the energy barrier for the HER. This theoretical result aligns closely with the experimental findings, confirming that the $NiSe_2$@NiFe-PBA heterostructure significantly enhances catalytic activity. Additionally, the charge transfer mechanism in $NiSe_2$@NiFe-PBA was investigated through a differential charge density analysis. In Figure 8i, the yellow regions represent charge accumulation, while the cyan regions indicate charge depletion. Ni and Fe atoms preferentially lose electrons, adopting positive oxidation states, whereas Se and N atoms accumulate electrons, forming negative charge states. Stronger charge transfer occurs at the $NiSe_2$@NiFe-PBA heterointerface, contributing to its superior HER catalytic performance. To explore the OER reaction mechanism and identify the rate-determining step (RDS), Gibbs free energy changes (ΔG) for each reaction step were calculated under zero-potential conditions (U = 0 V). As shown in Figure 8j, the step where O reacts with H_2O to form an OOH (ΔG_3) exhibits a free energy change of 1.74 eV for $NiSe_2$@NiFe-PBA/NF, significantly higher than the ΔG_3 of 1.10 eV for $NiSe_2$/Ni−Fe_2P/NF, indicating that the latter system has a lower reaction barrier in this step. Furthermore, for $NiSe_2$/Ni−Fe_2P/NF, the second reaction step (OH* → O*) shows the highest ΔG_2 of 1.45 eV, making it the RDS. In contrast, the RDS for $NiSe_2$@NiFe-PBA/NF corresponds to the third step (ΔG_3 = 1.74 eV). Since the RDS barrier of $NiSe_2$/Ni−Fe_2P/NF (1.45 eV) is significantly lower than that of $NiSe_2$@NiFe-PBA/NF (1.74 eV), the former system exhibits superior OER performance. These theoretical calculations confirm that the $NiSe_2$/Ni−Fe_2P/NF heterostructure formed through vapor-phase phosphidation optimizes the reaction pathway and reduces the energy barriers of critical steps, thereby enhancing the OER activity. This conclusion is consistent with our experimental results.

To further evaluate the practical potential of the prepared catalysts for overall water-splitting applications, we constructed an integrated water electrolysis cell using $NiSe_2$/Ni−Fe_2P/NF as both the anode and cathode bifunctional electrodes (Figure 9a). Under 1.0 M KOH electrolyte conditions, linear sweep voltammetry (LSV) measurements (Figure 9b) demonstrated that this electrolyzer required only 1.885 V to achieve a current density of 100 mA cm^{-2}, significantly lower than those assembled with $NiSe_2$/NF (1.941 V) and Ni−Fe_2P/NF (1.896 V). This result confirms the superior bifunctional catalytic activity and reduced total overpotential of $NiSe_2$/Ni−Fe_2P/NF. In a simulated alkaline seawater environment (1 M KOH + seawater) (Figure 9c), the $NiSe_2$/Ni−Fe_2P/NF electrolyzer maintained excellent performance, requiring only 1.854 V at 100 mA cm^{-2} while sustaining low voltage demands at higher current densities, highlighting its strong industrial application potential. Cycling stability is a critical metric for assessing catalyst practicality. As shown in Figure 9d, the $NiSe_2$/Ni−Fe_2P/NF electrolyzer exhibited minimal voltage decay after 200 h of continuous operation at 160 mA cm^{-2}, demonstrating exceptional long-term stability in both 1 M KOH and 1 M KOH + seawater environments. However, comparison of performance changes between the two electrolytes revealed a slight voltage increase in seawater containing Cl^- and Na^+ impurity ions, indicating that these ions slightly affect the interfacial mass transfer and reaction kinetics. Further structural stability analysis through pre- and postcycling LSV curves (Figure 9e,f) showed nearly no voltage degradation in 1 M KOH, confirming the catalyst's structural integrity during prolonged operation. In contrast, the 1 M KOH + seawater system exhibited minor voltage degradation after 200 h, suggesting that seawater impurities may induce surface corrosion or active site passivation. Nevertheless, the system retained high catalytic activity, a testament to the efficient interfaces formed in the $NiSe_2$/Ni−Fe_2P/NF heterostructure, which enhances charge transport and structural robustness under harsh conditions. Additionally, to evaluate the application potential of $NiSe_2$@NiFe-PBA/NF in practical devices, we fabricated an anion-exchange membrane (AEM)-based electrolyzer using $NiSe_2$@NiFe-PBA/NF (1.0 cm × 1.0 cm) as bifunctional electrodes (Figure 9g). As shown in Figure 9h, the symmetric $NiSe_2$@NiFe-PBA/NF||$NiSe_2$@NiFe-PBA/NF electrolyzer achieved 10 mA cm^{-2} at only 1.573 V, significantly outperforming the $NiSe_2$/NF||$NiSe_2$/NF system, which required 1.662 V. Collectively, both $NiSe_2$/Ni−Fe_2P/NF and $NiSe_2$@NiFe-PBA/NF demonstrate excellent catalytic

https://doi.org/10.1021/acsami.5c14223
ACS Appl. Mater. Interfaces 2025, 17, 64340−64353

activity and stability for overall water splitting, particularly exhibiting low voltage requirements and high durability in practical electrolysis devices. These results fully validate their significant application prospects in green hydrogen production technologies, especially in alkaline water and direct seawater electrolysis systems.

4. CONCLUSIONS

This study presents a self-sacrificing template strategy based on $NiSe_2$ to construct a three-dimensional nanocube-assembled $NiSe_2$/Ni−Fe_2P/NF spherical structure for alkaline water and seawater electrolysis. The material demonstrates exceptional OER performance in both 1.0 M KOH and alkaline seawater environments, achieving current densities of 100 mA cm^{-2} at overpotentials of 263 and 281 mV, with corresponding Tafel slopes of 38 and 42.27 mV dec^{-1}, respectively. In water-splitting applications, the $NiSe_2$/Ni−Fe_2P/NF-based electrolyzer requires only 1.885 and 1.854 V to drive 100 mA cm^{-2} in 1.0 M KOH and alkaline seawater, respectively, maintaining stable operation for 100 h, thereby validating its durability under practical electrolytic conditions. Additionally, HER performance evaluation reveals that the $NiSe_2$@NiFe-PBA/NF sample exhibits outstanding hydrogen evolution activity, requiring only a 168 mV overpotential to achieve −10 mA cm^{-2} in 1.0 M KOH. DFT calculations demonstrate that compared to pure $NiSe_2$, the $NiSe_2$@NiFe-PBA heterostructure significantly enhances the atomic density of states near the Fermi level, with improved charge transfer capability at the interface.

■ ASSOCIATED CONTENT

Supporting Information

The Supporting Information is available free of charge at https://pubs.acs.org/doi/10.1021/acsami.5c14223.

Characterization of $Ni(OH)_2$/NF and $NiSe_2$/NF samples; SEM images of $Ni(OH)_2$ sample; TEM images and EDS mapping of $NiSe_2$/NF sample; overpotential plot in 1 M KOH and in 1 M KOH + seawater; and electrocatalytic OER performance comparison of the samples. (PDF)

■ AUTHOR INFORMATION

Corresponding Authors

Depeng Zhao − *School of New Energy, Shenyang Institute of Engineering, Shenyang 110136, P. R. China; School of Materials Science and Engineering, Liaoning University of Technology, Jinzhou 121000 Liaoning, P. R. China;* orcid.org/0000-0001-8054-3926; Email: hellodepeng@163.com

Rongda Zhao − *School of New Energy, Shenyang Institute of Engineering, Shenyang 110136, P. R. China; School of Materials Science and Engineering, Liaoning University of Technology, Jinzhou 121000 Liaoning, P. R. China;* orcid.org/0000-0002-1637-0909; Email: rongdazhaoln@126.com

Lihua Miao − *School of Medical Information Engineering, Shenyang Medical College, Shenyang 110043 Liaoning, P. R. China*; Email: miaolihua@163.com

Authors

Huiya Zhou − *School of New Energy, Shenyang Institute of Engineering, Shenyang 110136, P. R. China; School of Materials Science and Engineering, Liaoning University of Technology, Jinzhou 121000 Liaoning, P. R. China*

Xin Li − *School of Materials Science and Engineering, Liaoning University of Technology, Jinzhou 121000 Liaoning, P. R. China*

Boyao Zhang − *School of Materials Science and Engineering, Liaoning University of Technology, Jinzhou 121000 Liaoning, P. R. China*

Heran Ren − *School of Materials Science and Engineering, Liaoning University of Technology, Jinzhou 121000 Liaoning, P. R. China*

Complete contact information is available at: https://pubs.acs.org/10.1021/acsami.5c14223

Notes

The authors declare no competing financial interest.

■ ACKNOWLEDGMENTS

This work was supported by the National Natural Science Foundation of China (No. 51971106), the Project of Education Department of Liaoning Province (No. LJKMZ20220959), and the Science and Technology Innovation Talent Project of Liaoning Provincial Department of Education (LJ222411632049).

■ REFERENCES

(1) Bai, M.; Ai, T.; Bao, W.; Han, J.; Zhang, J.; Yu, Q.; Liu, J.; Wei, X.; Zou, X.; Feng, L. Modulating electronic structure of nickel diselenide by vanadium doping toward highly efficient and stable bifunctional electrocatalysts for overall water splitting. *J. Mater. Sci. Technol.* **2024**, *187*, 63−71.

(2) Dou, Y.; He, C.-T.; Zhang, L.; Yin, H.; Al-Mamun, M.; Ma, J.; Zhao, H. Approaching the activity limit of $CoSe_2$ for oxygen evolution via Fe doping and Co vacancy. *Nat. Commun.* **2020**, *11* (1), No. 1664.

(3) Jiang, Y.; Gao, S.; Liu, X.; Wang, Y.; Zhou, S.; Liu, Q.; Abdukayum, A.; Hu, G. Recent achievements in selenium-based transition metal electrocatalysts for pH-universal water splitting. *Nano Res.* **2024**, *17* (7), 5763−5785.

(4) Li, W.; Niu, Y.; Wu, X.; Wu, F.; Li, T.; Hu, W. Heterostructured $CoSe_2$/$FeSe_2$ Nanoparticles with Abundant Vacancies and Strong Electronic Coupling Supported on Carbon Nanorods for Oxygen Evolution Electrocatalysis. *ACS Sustainable Chem. Eng.* **2020**, *8* (11), 4658−4666.

(5) Zhang, X.-L.; Hu, S.-J.; Zheng, Y.-R.; Wu, R.; Gao, F.-Y.; Yang, P.-P.; Niu, Z.-Z.; Gu, C.; Yu, X.; Zheng, X.-S.; Ma, C.; Zheng, X.; Zhu, J.-F.; Gao, M.-R.; Yu, S.-H. Polymorphic cobalt diselenide as extremely stable electrocatalyst in acidic media via a phase-mixing strategy. *Nat. Commun.* **2019**, *10* (1), No. 5338.

(6) Zhao, Y.; Jin, B.; Zheng, Y.; Jin, H.; Jiao, Y.; Qiao, S. Z. Charge State Manipulation of Cobalt Selenide Catalyst for Overall Seawater Electrolysis. *Adv. Energy Mater.* **2018**, *8* (29), No. 1801926.

(7) Zhou, H.; Yu, F.; Liu, Y.; Sun, J.; Zhu, Z.; He, R.; Bao, J.; Goddard, W. A.; Chen, S.; Ren, Z. Outstanding hydrogen evolution reaction catalyzed by porous nickel diselenide electrocatalysts. *Energy Environ. Sci.* **2017**, *10* (6), 1487−1492.

(8) Zhang, J.; Zhang, S.; Zhang, Z.; Wang, J.; Zhang, Z.; Cheng, G. NiFeCo selenide nanosheets as promising electrocatalysts for oxygen evolution reaction. *J. Alloys Compd.* **2023**, *939*, No. 168753.

(9) Hou, M.; Gong, S.; Ji, L.; Huang, J.; Xu, M.; Chen, Z. Three-dimensional porous ultrathin carbon networks reinforced PBAs-derived electrocatalysts for efficient oxygen evolution. *Chem. Eng. J.* **2021**, *419*, No. 129575.

(10) Ji, Y.-R.; Guo, Y.-F.; Liu, X.; Wang, P.-F.; Yi, T.-F. Insights on rational design and regulation strategies of Prussian blue analogues and their derivatives towards high-performance electrocatalysts. *Chem. Eng. J.* **2023**, *471*, No. 144743.

(11) Lee, M. G.; Kim, S.; Lee, Y. Direct seawater electrolysis: Breaking the dependency on noble metal-based electrocatalysts. *Int. J. Hydrogen Energy* **2025**, *130*, 89−107.
(12) Zhang, H.-M.; Zuo, L.; Li, J.; Zhang, S.; Guo, J.; Li, X.-P.; Liu, G.; Wang, P.; Sun, J. Research and strategies for efficient electrocatalysts towards anodic oxygen evolution reaction in seawater electrolysis system. *J. Mater. Sci. Technol.* **2024**, *187*, 123−140.
(13) Zhang, B.-Y.; Xu, S.-L.; Li, J.; Zhou, H.-Y.; Li, X.; Zhao, R.-D.; Wu, F.-F.; Zhao, D. Excellent electrocatalytic performance of CuCo2S4 nanowires for high-efficiency overall water splitting in alkaline and seawater media. *CrystEngComm* **2025**, *27* (22), 3700−3711.
(14) Yu, H.; Wan, J.; Goodsite, M.; Jin, H. Advancing direct seawater electrocatalysis for green and affordable hydrogen. *One Earth* **2023**, *6* (3), 267−277.
(15) Zhou, H.; Zhang, Z.; Zhang, Q.; Zhang, B.; Li, X.; Xu, S.-L.; Zhao, R.-D.; Zhao, X.; Zhao, D.-P.; Li, M.; Wu, F.-F. Multidimensional Engineering Strategies for Transition Metal Selenide Electrocatalysts in Water Electrolysis with Performance Optimization Mechanisms and Future Perspectives. *Chem. Rec.* **2025**, *25* (8), No. e202500082.
(16) Li, W.-J.; Han, C.; Cheng, G.; Chou, S.-L.; Liu, H. K.; Dou, S.-X. Chemical Properties, Structural Properties, and Energy Storage Applications of Prussian Blue Analogues. *Small* **2019**, *15* (32), No. 1900470.
(17) Jiang, M.; Fan, X.; Cao, S.; Wang, Z.; Yang, Z.; Zhang, W. Thermally activated carbon−nitrogen vacancies in double-shelled NiFe Prussian blue analogue nanocages for enhanced electrocatalytic oxygen evolution. *J. Mater. Chem. A* **2021**, *9* (21), 12734−12745.
(18) Muthurasu, A.; Ko, T. H.; Kim, T. W.; Chhetri, K.; Kim, H. Y. Interfacial Electronic Modification of Nickel Phosphide via Iron Doping: An Efficient Bifunctional Catalyst for Water/Seawater Splitting. *Adv. Funct. Mater.* **2024**, *34* (41), No. 2404254.
(19) Tarigan, A. M.; Rinawati, M.; Aulia, S.; Chang, L. Y.; Chang, C. Y.; Su, W. N.; Haw, S. C.; Huang, W. H.; Setyawan, H.; Yeh, M. H. Dual-Driven Activation of High-Valence States in Prussian Blue Analogues Via Graphene-Quantum Dots and Ozone-Induced Surface Restructuring for Superior Hydrogen Evolution Electrocatalyst. *Small Methods* **2025**, *9* (5), No. 2401708.
(20) Zhang, S.; Cheng, Y.; Ni, Z.; Lei, X.; Wang, B.; Liu, X.; Guo, R. Preparation of hollow CoFe Prussian blue analogues and their derived CoP-FeP nanoboxes as efficient electrocatalysts as oxygen evolution reactions. *J. Power Sources* **2024**, *623*, No. 235454.
(21) Xu, X.; Mo, Q.; Zheng, K.; Xu, Z.; Cai, H. Multifunctional Ni_3S_2@NF-based electrocatalysts for efficient and durable electrocatalytic water splitting. *Dalton Trans.* **2023**, *52* (35), 12378−12389.
(22) Li, D.; Zhang, Z.-F.; Yang, Z.-Y.; Wu, W.-Y.; Zhang, M.-H.; Yang, T.-R.; Zhang, Q.-S.; Xie, J.-Y. Ni3P-Ni heterostructure electrocatalyst for alkaline hydrogen evolution. *J. Alloys Compd.* **2022**, *921*, No. 166204.
(23) Li, Y.; Du, H.; Su, Y.; Zhao, J.; Qu, K.; Zhang, X.; Zhang, Y.; Dong, Y.; Guo, Z. Construction of Heterostructured NiS/$NiSe_2$ and their application in electrocatalytic water splitting. *Int. J. Hydrogen Energy* **2024**, *66*, 286−293.
(24) Ding, X.; Zhang, M.; Chang, X.; Zhou, X. In situ growth of Prussian blue analogue-derived Fe-doped NiS on $Ni(OH)_2$ for efficient hydrogen evolution reaction. *Dalton Trans.* **2023**, *52* (6), 1680−1686.
(25) Sivagurunathan, A. T.; Kavinkumar, T.; Kim, D.-H. Interfacial charge density modulated Fe_2P/MoO_2 heterojunction as an efficient bidirectional electrocatalyst towards exceptional electrocatalytic water splitting. *J. Alloys Compd.* **2025**, *1012*, No. 178468.
(26) Ramesh, S. K.; Son, J.; Ganesan, V.; Kim, J. Carbon-incorporated Ni_2P-Fe_2P hollow nanorods as superior electrocatalysts for the oxygen evolution reaction. *Nanoscale* **2022**, *14* (43), 16262−16269.
(27) Bai, Y.; Wang, Y.; Qiao, Z.; Yang, Y.; Deng, L.; Li, C.; Chen, X.; Wang, S.; Huang, Y.; Zhang, X.; Cao, D. Facile synthesis of Fe_2P/Co embedded trifunctional electrocatalyst for high-performance anion exchange membrane fuel cells, rechargeable Zn−air batteries, and overall water splitting. *J. Mater. Chem. A* **2022**, *10* (30), 16037−16045.
(28) Gao, J.; Ma, H.; Luo, X.; Yu, L.; Gu, X.; Liu, J. Boosting electrocatalytic activity of $NiSe_2$ nanosheets by anion-cation dual-doping for highly efficient hydrogen evolution reaction. *J. Alloys Compd.* **2023**, *933*, No. 167793.
(29) Zhang, L.; Wang, T.; Sun, L.; Sun, Y.; Hu, T.; Xu, K.; Ma, F. Hydrothermal synthesis of 3D hierarchical $MoSe_2/NiSe_2$ composite nanowires on carbon fiber paper and their enhanced electrocatalytic activity for the hydrogen evolution reaction. *J. Mater. Chem. A* **2017**, *5* (37), 19752−19759.
(30) Zhu, D.; Liu, G.; Zhang, G.; Yin, Z.; Yang, H.; Gao, S.; Zhang, C.; Xi, X. Oxygen vacancy induced construction of $NiCo_2O_4/NiSe_2$ heterostructure electrocatalyst for high-efficiency oxygen evolution reaction. *J. Colloid Interface Sci.* **2025**, *693*, No. 137648.
(31) Chang, B.; Ren, Y.; Mu, N.; Zuo, S.; Zou, C.; Zhou, W.; Wen, L.; Tao, H.; Zhou, W.; Lai, Z.; Kobayashi, Y.; Zhang, H. Dynamic Redox Induced Localized Charge Accumulation Accelerating Proton Exchange Membrane Electrolysis. *Adv. Mater.* **2025**, *37* (7), No. 2405447.
(32) Huang, J.; Sullivan, N. P.; Zakutayev, A.; O'Hayre, R. How reliable is distribution of relaxation times (DRT) analysis? A dual regression-classification perspective on DRT estimation, interpretation, and accuracy. *Electrochim. Acta* **2023**, *443*, No. 141879.
(33) Zhao, Y.; Kücher, S.; Jossen, A. Investigation of the diffusion phenomena in lithium-ion batteries with distribution of relaxation times. *Electrochim. Acta* **2022**, *432*, No. 141174.
(34) Luo, X.; Ji, P.; Wang, P.; Tan, X.; Chen, L.; Mu, S. Spherical Ni_3S_2/Fe-NiPx Magic Cube with Ultrahigh Water/Seawater Oxidation Efficiency. *Adv. Sci.* **2022**, *9* (7), No. 2104846.
(35) Liu, X.; Meng, J.; Zhu, J.; Huang, M.; Wen, B.; Guo, R.; Mai, L. Comprehensive Understandings into Complete Reconstruction of Precatalysts: Synthesis, Applications, and Characterizations. *Adv. Mater.* **2021**, *33* (32), No. 2007344.
(36) Rahmati, Z.; Roushani, M.; Hosseini, H. Ir/Co/$NiSe_2$ Nanocages as High-Performance Electrocatalysts for Water Splitting and Sensors. *ACS Appl. Nano Mater.* **2024**, *7* (5), 5564−5575.
(37) Pan, Y.; Ma, X.; Wang, M.; Yang, X.; Liu, S.; Chen, H.-C.; Zhuang, Z.; Zhang, Y.; Cheong, W.-C.; Zhang, C.; Cao, X.; Shen, R.; Xu, Q.; Zhu, W.; Liu, Y.; Wang, X.; Zhang, X.; Yan, W.; Li, J.; Chen, H. M.; Chen, C.; Li, Y. Construction of N, P Co-Doped Carbon Frames Anchored with Fe Single Atoms and Fe_2P Nanoparticles as a Robust Coupling Catalyst for Electrocatalytic Oxygen Reduction. *Adv. Mater.* **2022**, *34* (29), No. 2203621.
(38) Wang, X.; Wang, B.; Chen, Y.; Wang, M.; Wu, Q.; Srinivas, K.; Yu, B.; Zhang, X.; Ma, F.; Zhang, W. Fe_2P nanoparticles embedded on Ni_2P nanosheets as highly efficient and stable bifunctional electrocatalysts for water splitting. *J. Mater. Sci. Technol.* **2022**, *105*, 266−273.
(39) Chen, W.; Chen, S.; Guo, M.; Jiang, X.; Xia, J.; Chen, M.; Xiong, Y.; Qian, X. Fe_2P-coated Ni_2P/Co_2P yolk-shelled porous nanospheres as advanced Pt-free electrocatalysts for efficient pH-universal hydrogen evolution. *Int. J. Hydrogen Energy* **2024**, *78*, 851−860.
(40) Nguyen, A. N.; Rosyadi, A. F.; Kim, D.; Yoo, H. Hierarchical Selenium-Doped Nickel−Cobalt Hybrids on Carbon Paper for the Overall Water-Splitting Electrocatalytic System. *ACS Appl. Mater. Interfaces* **2025**, *17* (4), 6428−6440.
(41) Liu, Y.; Hu, Y.; Zhao, X.; Zhu, S.; Min, Y.; Xu, Q.; Li, Q. Oxygen Vacancy and Heterostructure Modulation of Co_2P/Fe_2P Electrocatalysts for Improving Total Water Splitting. *ACS Appl. Mater. Interfaces* **2024**, *16* (11), 13795−13805.
(42) Zhao, D.; Liu, X.; Zhang, W.-C.; Wu, X.; Cho, Y.-R. Highly Efficient and Stable Mo-CoP_3@FeOOH Electrocatalysts for Alkaline Seawater Splitting. *Small Methods* **2024**, *8* (9), No. 2301474.
(43) Tang, Y.; Shen, K.; Zheng, J.; He, B.; Chen, J.; Lu, J.; Ge, W.; Shen, L.; Yang, P.; Deng, S. d-Band center modulating of CoOx/

Co_9S_8 by oxygen vacancies for fast-kinetics pathway of water oxidation. *Chem. Eng. J.* **2022**, *427*, No. 130915.

https://doi.org/10.1021/acsami.5c14223
ACS Appl. Mater. Interfaces 2025, 17, 64340−64353